Applied Surface Science 599 (2022) 153915

Contents lists available at ScienceDirect

Applied Surface Science

journal homepage: www.elsevier.com/locate/apsusc

Full Length Article

Phosphorus doped carbon nanosheets encapsulated Cu_3P heterostructure for superior lithium storage by experimental verification and first-principles calculation

Tianlin Li [a], Quantao Feng [a], Tongde Wang [a], Yanwei Sui [a,*], Haiting Chen [b], Liping Ding [b], Eugene B. Chubenko [c], Vitaly Bondarenko [c], Xiujuan Feng [d,e], Wen Zhang [f], Peng Cao [f]

[a] Jiangsu Province Engineering Laboratory of High Eicient Energy Storage Technology and Equipments, School of Materials Science and Physics, China University of Mining and Technology, Xuzhou 221116, PR China
[b] Shandong Shengquan New Energy Technology Co, Ltd, Jinan 250000, PR China
[c] Micro- and Nanoelectronics Department, Belarusian State University of Informatics and Radioelectronics, Minsk 220013 Belarus
[d] School of Mines, China University of Mining and Technology, Xuzhou 221116, PR China
[e] Mechano Chemistry Research Institute, China University of Mining and Technology, Xuzhou 221116, PR China
[f] Department of Chemical & Materials Engineering, University of Auckland, Auckland 1142, New Zealand

ARTICLE INFO

Keywords:
Cu_3P
Phosphorus doped carbon nanosheets
Lithium storage
Density Function Theory

ABSTRACT

As a transition metal phosphide, copper phosphide (Cu_3P) undergoes high volume expansion and reduced electrical conductivity during cycling, causing kinetic issues and rapid capacity fading. The well-dispersed and sheet-like structure of individual nano-copper phosphide particles is crucial for alleviating volume expansion and enhancing kinetic behavior, which however have been rarely concerned. In this work, we report a novel heterostructure with nano-copper phosphide particles immobilized on phosphorus doped carbon nanosheet (Cu_3P@PCNSs) by using Cu-BDC as the precursor. When the synthesis temperature is 600 °C, the Cu_3P@PCNSs-600 exhibits a remarkable rate capability (383.4 mA h g^{-1} at 2 A g^{-1}) and outstanding long-term durability (436.4 mA h g^{-1} at 1000 mA g^{-1} after 1000 cycles) for lithium storage. The monodisperse structure of Cu_3P nanoparticles embedded in phosphorus doped carbon could reduce the volume change of Cu_3P nanoparticles. Moreover, the electron density, adsorption energy, diffusion barrier and other properties of Cu_3P and carbon matrix heterostructures were calculated in accordance with density functional theory (DFT). As dndicated by the calculation, the strong interaction between the heterostructures had an effect on the adsorption capacity of Li, and the experimental results were confirmed to be correct. This novel Cu_3P@PCNSs electrode can be used as an effective strategy for applying other transition metal electrode materials in lithium-ion batteries.

1. Introduction

As portable electronic and electric vehicles have been increasingly demanded, lithium-ion rechargeable batteries (LIBs) characterized by high specific capacity and excellent circulation performance have tended to be the focus of research [1–3]. But graphite, the commercial anode material, has a correspondingly inferior theoretical capacity (372 mAh g^{-1}), which represents a lower voltage platform and shows safety risks. To meet the requirement of higher energy density, alternative anode materials should be urgently found (e.g., transition metal oxides and transition metal phosphates) [4–7]. Among the above materials, transition metal phosphates (TMPs) have been recognized as the candidate anode materials for the next generation of lithium-ion batteries since they are characterized by excellent theoretical specific capacity (500–2000 mA h g^{-1}) and high electrochemical activity. To be specific, Cu-based phosphating compounds, especially Cu_3P, have been extensively concerned [8]. Cu_3P has a theoretical weight capacity of 363 mA h g^{-1}, whereas, its volume (3020 mA h cm^{-3}) is nearly threefold that of graphite (830 mA h cm^{-3}) due to its considerable material density [9]. At present, nano-crystal agglomeration and poor conductivity are common in the synthesized Cu_3P, thus significantly impacting the electrical conductivity and charge/discharge rate of the materials [10,11]. Three main strategies can be used to improve the above defects: (1) to change the morphology at the nanoscale [12,13], for example, to

* Corresponding author.
E-mail address: wyds123456@outlook.com (Y. Sui).

https://doi.org/10.1016/j.apsusc.2022.153915
Received 21 March 2022; Received in revised form 30 May 2022; Accepted 5 June 2022
Available online 11 June 2022

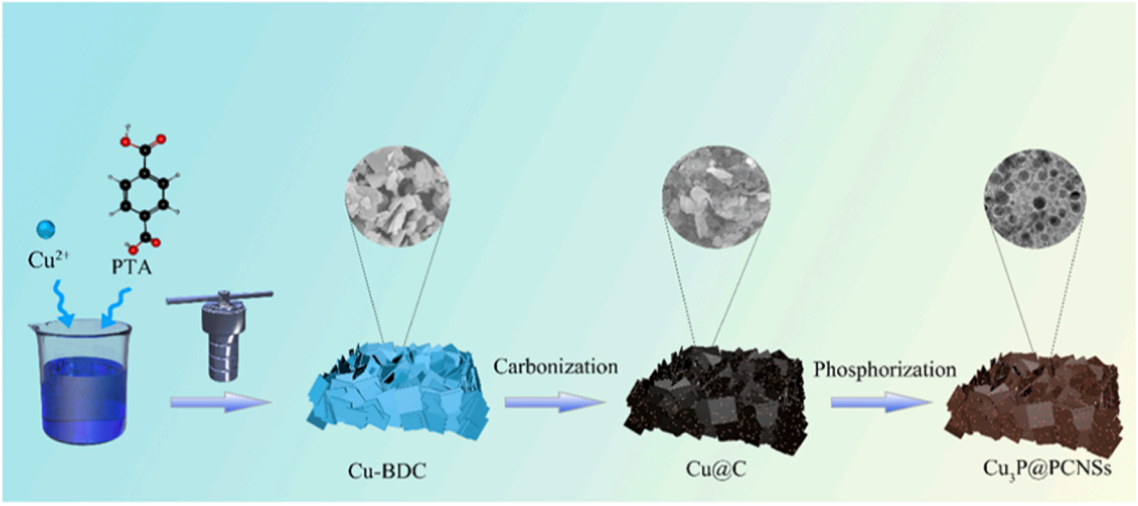

Fig. 1. Preparation flow chart of 2D Cu_3P@PCNSs composites.

synthesize Cu_3P with different morphologies (e.g., nanowires [14], nanoplates [15], octahedron [16] and nanoribbons [17]); (2) composite with carbon matrix materials [18]. Carbon materials have been reported as a type of highly popular anode materials due to their large specific surface area, supernal porosity and chemical stability [19]. More importantly, carbon-based materials are capable of inhibiting the agglomeration of nano-metal/transition metal compound particles [5,20,21]. (3) Heteratomic doping plays a crucial role in improving the electronic properties exhibited by materials. For example, N doping can provide stable configuration for silicon nanoparticles and improve the electrical conductivity of electrodes [22]. Through the synthesis 2D nitrogen-rich C/Si composites, lithium ion battery anode materials exhibiting high cycling performance can be prepared. Therefore, it is very necessary to prepare novel electrode material with Cu_3P nanoparticles encapsulated in 2D carbon matrix.

Metal-organic skeleton (MOF) materials refer to organic–inorganic hybrid materials that are formed by organic ligands and metal ions through coordination bonds [23,24]. They are characterized by excellent porosity and considerable detailed surface area, and their morphologies are diversified and controllable. They have been applied in a considerable number of fields (e.g., solar cells, electrocatalysis and lithium ion batteries) [25,26]. For instance, nickel-based MOF was found to have excellent capacitance dealing in KOH aqueous electrolyte, with a worthy specific capacitance of 726F g^{-1} [27]. $SnCl_2$ was adsorbed in the HKUST-1 channel and then calcined to prepare SnO_2@C composite materials, which served as the anode materials for lithium ion batteries [28]. Thus, MOF material is expected to be an outstanding candidate material for the next generation of electrode materials. In this study, Cu-BDC was used as a precursor, octahedral shape was prepared through hydrothermal Cu-MOF. Moreover, carbon-coated octahedral Cu_3P nanoparticles were obtained through the calcination of coking and phosphating. Furthermore, the cycle of the material had high stability and rate performance, much better than pristine Cu_3P, so it is expected to be high-performance anode electrode material of lithium ion batteries.

A vital question is how Li adsorption can be improved in heterogeneous structures. Most of the existing studies have focused on synthetic materials and experimental trial-and-error direction to further the property of electrode materials [29], and the DFT calculation can present systematical insights into the mechanism of lithium storage structure [30]. Accordingly, further theoretical research on heterostructures of hetero-atom doped carbon and Cu_3P at a molecular level should be conducted. In this study, the properties of adsorption energy, state density and diffusion barrier of the phosphorus-doped carbon matrix and Cu_3P heterostructure (Cu_3P@PCNSs) were calculated and analyzed in accordance with density functional theory (DFT). As indicated by the calculated results, there was a significant electron interaction between the heterostructures. Compared with Cu_3P, Cu_3P@PCNSs was characterized by more excellent adsorption energy and a smaller diffusion barrier. The accuracy of the experiment was verified. This study presented a novel research idea for preparing Cu_3P@Phosphorus doped carbon heterostructure anode materials with high cycling and rate capability.

2. Experimental section

2.1. Preparation of Cu-BDC

The Cu-BDC was synthesized by a hydrothermal method. First, 1.8 mmol Phthalic acid (PTA) and 2.0 mmol $Cu(NO_3)_2{\cdot}3H_2O$ were dissminatived in 40 mL N, N-dimethylformamide solution (DMF). Then, 40 mL acetonitrile (CH_3CN) solution was added to the above solution and stirred continuously for 10 min. Lastly, the solution was transferred to a 100 mL TEflon lined autoclave and then heated for 18 h at 120℃. After hydrothermal completion, the precipitates were collected via centrifugation (DMF and methanol were washed three times), and the centrifuged blue precipitates were freeze-dried for 48 h.

2.2. Preparation of Cu_3P@PCNSs

The freeze-dried Cu-BDC blue powder was placed into the quartz boat and then calcined at 500℃, 600℃ and 700℃ respectively for 2 h at nitrogen gas, with a rate of rising of temperature at 2℃/min. After the cooling to indoor temperature in the tubular furnace, brown powder, i.e., Cu@C, could be obtained. Subsequently, two porcelain vessels were prepared, brown powder Cu@C was placed at the lower end of the tubular furnace, and sodium hypophosphate was placed at the upper end of the tubular furnace, in which the mass ratio of Cu@C and sodium hypophosphate was 1:10. The phosphating was perfomed at argon gas for 3 h, the calcination temperature was 300℃, and the heating rate was 2℃/min.

2.3. Preparation of Cu_3P

To illustrate the affection of phosphorus doping carbon on the electrochemical performance of Cu_3P, pure Cu_3P was prepared as a negative material as a comparison. The specific preparation method was the removal of the N_2 protection in the carbonization step, the calcination in the air to prepare pure CuO powder, the phosphating CuO at argon gas for 3 h, and then the phosphating at 300℃. The heating rate

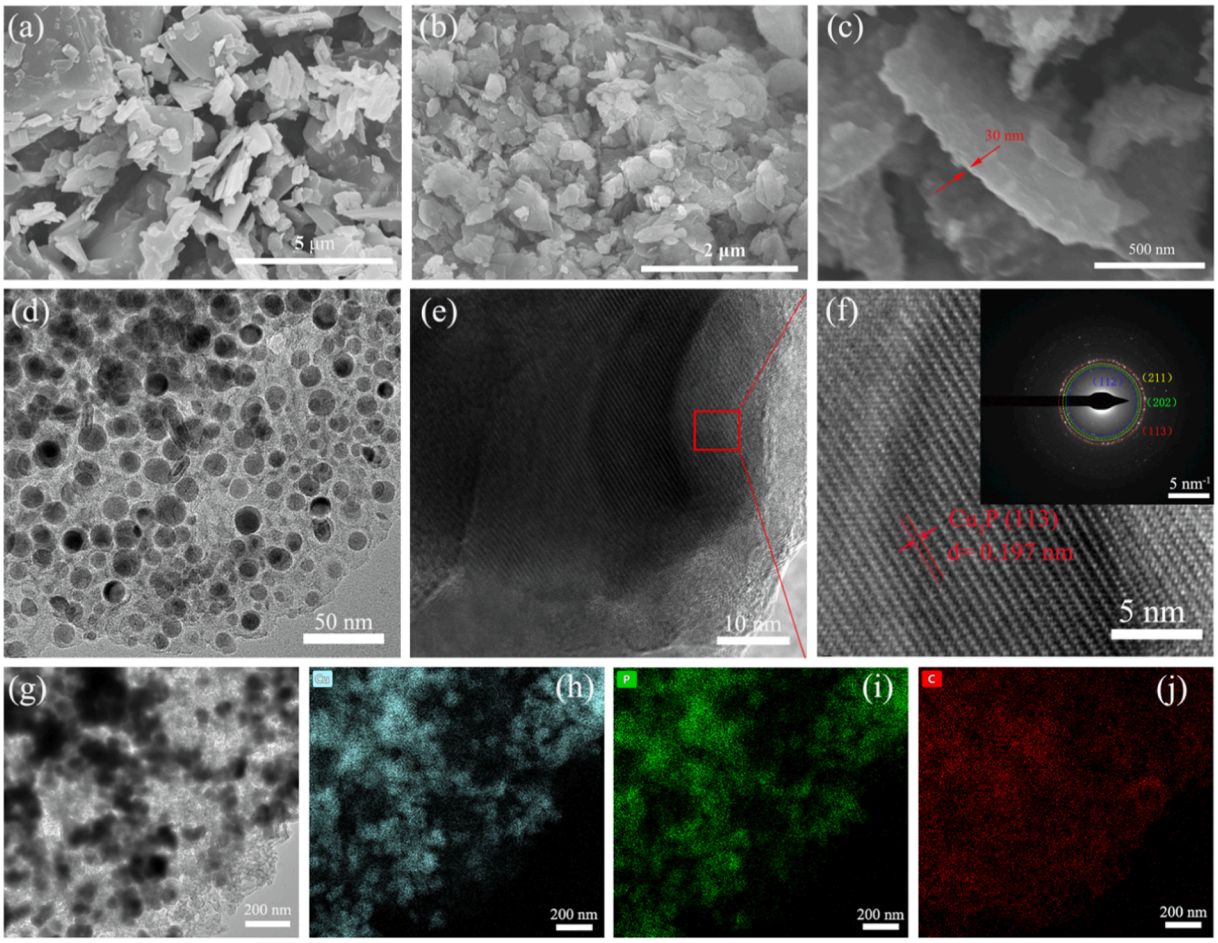

Fig. 2. (a) SEM images of Cu-BDC; (b-c) SEM images of Cu_3P@PCNSs-600; (d-e) TEM of Cu_3P@PCNSs-600; (g-j) EDS mapping of Cu_3P@PCNSs-600.

was 2 ℃/min.

2.4. DFT calculations

The First-principles calculations were conducted using the Vienna Ab-initio Simulation Package (VASP) software package [31,32]. Plane wave generator Project Augmented Wave (PAW) [33,34] pseudopotential was adopted to express the interaction between ion and electron, and the interaction of electron exchange was processed using Perdew-Burke-Ernzerhof (PBE) [35] functional of Generalized Gradient Approximation (GGA) [36]. The cutoff energy was set to 650 eV, and the force and energy convergence standards of each atom were 0.05 eV/Å and 10^{-5} eV, separately. To avoid the mutual influence between the atomic layers, the vacuum layer was set to 15 Å. Two models of Cu_3P and Cu_3P and phosphorus-doped carbon matrix heterostructure (Cu_3P@PCNSs) were built. The K-point network space of $3 \times 3 \times 1$ and $3 \times 4 \times 1$ was used to improve the structure of the model. The construction was completed using the vaspkit module based on the vasp software. The energy of elemental atoms was calculated in a $20 \times 20 \times 20$ Å unit cell. Furthermore, since the copper in the model was a transition metal element, the system contained strongly related d-orbital and f-orbital electrons, and their strong interaction would cause non-local problems of electrons, thus resulting in the understanding band gap. Thus, the DFT + U energy functional form was used to modify the model, so as to ensure the accuracy of the calculation [37,38].

3. Results and discussion

3.1. Structure and morphology characterization

We adopted a hydrothermal method and a two-step process of carbonization and phosphating to synthesize Cu_3P@PCNSs hybrid materials with tailored 2D nanosheets microstructures (illustrated in Fig. 1, and see the Experimental Section). Briefly, the 2D Cu-BDC nanosheets was first self-assembled by Cu^{2+} and PTA ligand via facile solvothermal method. Subsequently, the Cu-BDC was carbonized in nitrogen atmosphere to construct a 2D porous carbon nanosheets-encapsulated Cu nanoparticles (Cu@C). After phosphidation of the Cu@C with NaH_2PO_2 in argon flow, Cu@C is controllably converted into Cu_3P@PCNSs at 300 °C. The obtained Cu_3P nanoparticles are wrapped in a P doped carbon nanosheets.

The morphology and microstructure of the target product and the final Cu_3P@PCNSs synthetic were noticed by Scanning electron microscope and Transmission electron microscope. Fig. 2 shows the morphology of Cu-BDC precursor and the carbonized phosphating product Cu_3P@PCNSs-600 at 600℃. It can be seen from Fig. 2a that Cu-BDC has a 2D nanosheet with obvious irregular folding and relatively thin lamellae. As can be seen from Fig. 2b, when the carbonization temperature is 600℃, the product Cu_3P@PCNSs-600 retains a 2D sheet structure after phosphating, and the size of this layer was nearly 200 nm from Fig. 2c. Fig. 2d-f presents a TEM image of Cu_3P@PCNSs-600. According to Fig. 2d, the Cu_3P nanoparticles were uniformly loaded in the carbon substrate. As indicated by Fig. 2e, the surface of Cu_3P particles was coated with mofs-derived amorphous carbon, and the lattice fringes of Cu_3P particles were clearly observed in Fig. 2f. By calculating the

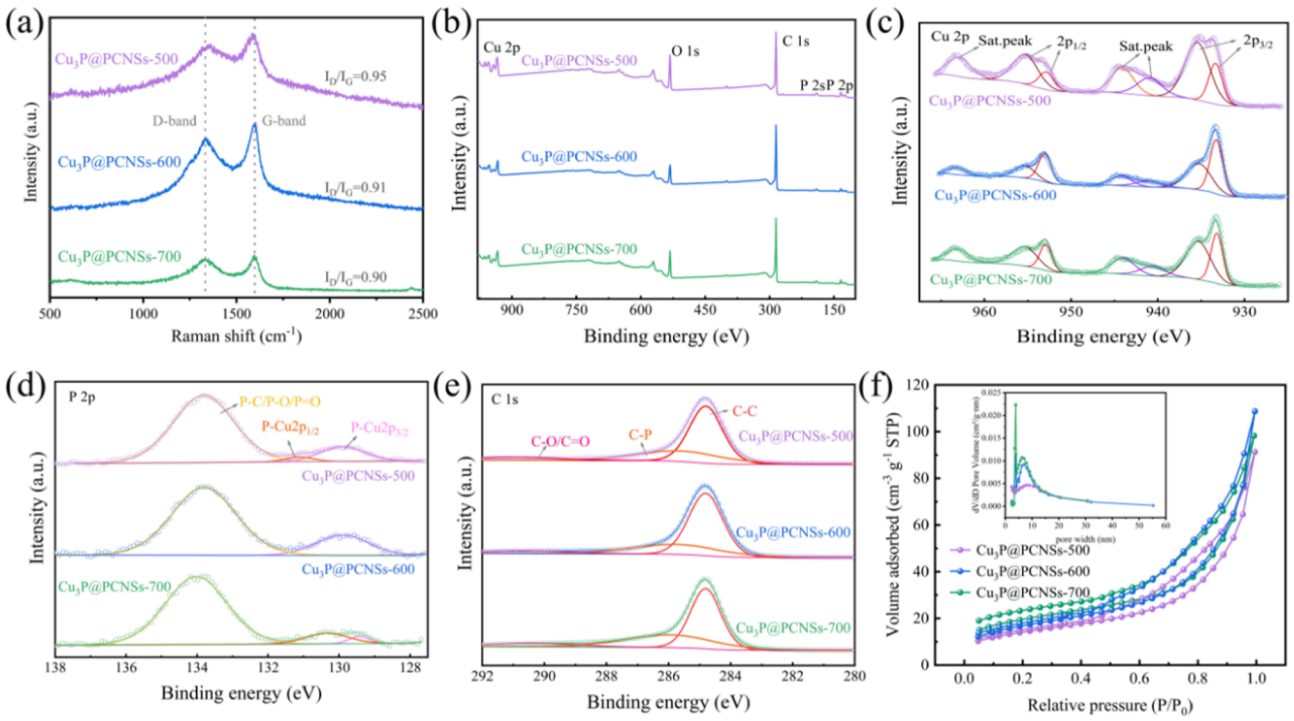

Fig. 3. a) Raman spectrum; (b) XPS survey spectra; (c-e) High-resolution XPD spectra of Cu 2P, P 2P and C 1S; (f) nitrogen adsorption–desorption isotherm of the Cu_3P@PCNSs-500, Cu_3P@PCNSs-600 and Cu_3P@PCNSs-700.

spacing of fringes, d = 0.197 nm, and combining with the data of PDF#71–2261, the corresponding crystal plane was determined as (1 1 3), corresponding to XRD. The special carbon outer structure was significantly conducive to reducing the electrode powdering attributed to the volume expansion of copper phosphide nanoparticles during the charging and discharging process. In addition, energy dispersion X-ray spectroscopy (EDX) mapping was conducted for the Cu_3P@PCNSs-600 sample, and Fig. 2g-j indicates that Cu, P and C elements were uniformly distributed on Cu_3P@PCNSs-600 nanosheets. It was further confirmed that Cu_3P@PCNSs-600 composite showed a 2D nanosheet structure with the characteristics of phosphorus doped carbon coated Cu_3P nanoparticles. To study the effect of temperature on material morphology, SEM images of Cu_3P@PCNSs-500 and Cu_3P@PCNSs-700 samples after phosphating at carbonization temperatures of 500℃ and 700℃ were generated, as presented in Fig. S1. According to the above figure, Cu_3P@PCNSs-500 also has a 2D sheet structure. Whereas, with the enhancement in the carbonization temperature, Cu will overgrow and form needle-like Cu_3P after phosphating. This needle-like structure is not conducive to the performance of the battery, and may puncture the diaphragm and cause battery short circuit.

Fig. S2a presents the crystal diffraction peak of hydrothermal synthesis of Cu-BDC and Cu@C. According to the above figure, after carbonization, under the protection of nitrogen inert gas, Cu-BDC heat treatment led to the formation of the composite structure of elemental Cu and carbon. The diffraction peak corresponds to the standard map of PDF#85–1326. Fig. S2b illustrates the XRD diffraction patterns of the three samples after carbonization at different temperatures (500, 600 and 700℃) and phosphatization. Moreover, the diffraction peaks of the three samples were all consistent with the standard card PDF#71–2261 of Cu_3P, and no other miscellaneous peaks were perceived in the diffraction peaks, thus indicating that the carbon here was amorphous carbon.

Raman spectroscopy was used to study the graphitization degree of Cu_3P@PCNSs, as presented in Fig. 3a. The two peaks of Raman spectroscopy were sp^3 disordered carbon (D band) related to atomic lattice defects at 1340 cm^{-1} and sp^2 graphitized carbon (G band) at 1587 cm^{-1}, representing the defect, disorder degree and graphitized structure, respectively [39]. The I_D/I_G ratios of Cu_3P@PCNSs-500, Cu_3P@PCNSs-600 and Cu_3P@PCNSs-700 were obtained as 0.95, 0.91 and 0.90, respectively. It was revealed that with the enhancement in the temperature, the material had fewer defects and a higher degree of graphitization, which could be conducive to reducing non-reversible capacity and increasing the performance of the battery. X-ray photoelectron spectroscopy was used to analyze the valence information of the three samples, and the data acquired from the test results are presented in Fig. 3b-e. The presence of Cu, P, C and O elements was observed in the full spectrum of XPS in Fig. 3b. Besides the composition of Cu_3P and C, the presence of oxygen elements was caused by the oxidation of the exposed surface of the sample in the air intake[40]. In the high-resolution atlas of Fig. 3c, 962.9 eV, 944.1 eV and 940.9 eV were considered the satellite peaks of Cu $2p^{3/2}$ and Cu $2p^{1/2}$, while 933.4 eV and 952.9 eV represent the peaks of Cu $2p^{3/2}$ and Cu $2p^{1/2}$ correlated with Cu-P bond, respectively. The peaks located at 935.5 eV and 955.4 eV could be considered as the peaks of Cu $2p^{3/2}$ and Cu $2p^{1/2}$ correlated with Cu-O bond[41]. The existence of Cu-O bond arose from surface oxidation of the material exposed to air, the retention of oxygen-containing functional groups of the material, as well as the oxidation of metal ions during carbonization. According to Fig. 3c, the peak of the Cu-O bond of Cu_3P@PCNSs-500 was higher than that of Cu_3P@PCNSs-600 and Cu_3P@PCNSs-700, thus indicating that lower carbonization temperature led to incomplete elimination of oxygen-containing functional groups in the precursor, while more oxygen atoms led to the increase in the irreversible capacity. Fig. 3d presents the high resolution spectrum of P_{2p} of the material. The peak of binding energy of 134.5 eV was P-O/P = O/P-C bond. The formation of P-O /P = O was primarily due to the oxidation of P. The characteristic peaks located at 130.5 eV and 128.9 eV represent P $2p^{1/2}$ and P $2p^{3/2}$, respectively, corresponding to the existence of the P-Cu bond, which further confirmed the successful synthesis of Cu_3P. The specific surface areas of Cu_3P@PCNSs-500, Cu_3P@PCNSs-600 and Cu_3P@PCNSs-700 samples were investigated using nitrogen adsorption/desorption method. The specific surface area of Cu_3P@PCNSs-600 (67.0 m^2 g^{-1}) was higher than that of

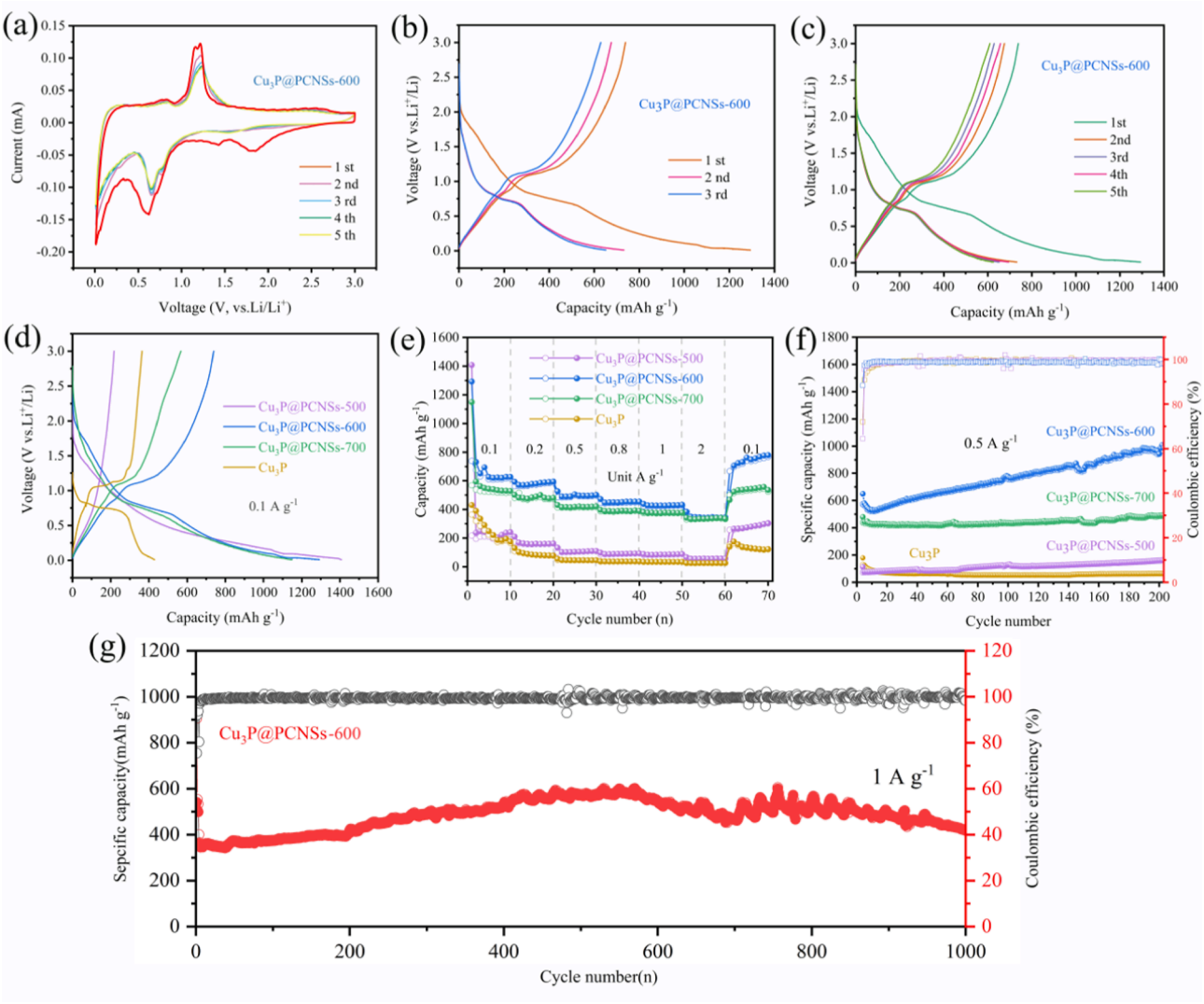

Fig. 4. (a) CV curves of Cu_3P@PCNSs-600 at a scan rate of 0.1 mV s^{-1}; (b-c) Galvanostratic Charge and discharge curves of Cu_3P@PCNSs-600 for the first three cycles/firtst five cycles; (d) First discharge/charfe curves of Cu_3P, Cu_3P@PCNSs-500, Cu_3P@PCNSs-600 and Cu_3P@PCNSs-700; (e) Rate performance at different current densities of Cu_3P, Cu_3P@PCNSs-500, Cu_3P@PCNSs-600 and Cu_3P@PCNSs-700; (f) Cycle performance of Cu_3P, Cu_3P@PCNSs-500, Cu_3P@PCNSs-600 and Cu_3P@PCNSs-700; (g) Long-term cycling performance of Cu_3P@PCNSs-600 at current densities of 1 A g^{-1} for 1000 cycles.

Cu_3P@PCNSs-500 (51.3 m^2 g^{-1}) and Cu_3P@PCNSs-700 (59.4 m^2 g^{-1}). The pore size distribution of the three samples rangeed from 1 to 15 nm (Fig. 3f). The rich specific surface area could significantly impact the rapid charge and discharge of the battery and improvethe high rate performance of the battery[42].

3.2. Electrochemical performance

Fig. S3a, Fig. 4a and Fig. S3c show CV curves of the first three cycles of Cu_3P@PCNSs-500, Cu_3P@PCNSs-600 and Cu_3P@PCNSs-700 samples, respectively, at a sweep speed of 0.1 mV s^{-1}. In the first scan of Fig. 4a, there are two wide reduction peaks at 2.0 V to 1.2 V, which disappeared in the subsequent scan since an electrolyte interface film (SEI) was formed on the surface of the electrode active material during the first charge and discharge[43]. When the current tended to increase, two reduction peaks appeare at 0.5 V and 0.75 V, thus indicating that the electrochemical lithium storage reaction took place in this range corresponding to the generation of $Li_XCu_{3-X}P$. In the first scanning phase, three anodic peaks are observed at 0.83 V, 1.15 V and 1.2 V, respectively, corresponding to the generation of $Li_{3-X}Cu_XP$ in the reversible delithium process. The good coincidence of the second and third scanning curves confirmed that the material had a high degree of invertibility. As indicated by the charge–discharge curves of the first three cycles of Cu_3P@PC NSs-600 sample at 0.1 A g^{-1} current density (Fig. 4b), under the condition of initial discharge, the short platform at 1.75 V represents the SEI formation process, and the long platform at 0.75 represents the reversible lithium embedding process. Two platforms represents the process of delithium at nearly 0.8 V and 1.2 V during the charging process, corresponding to the formation of CV curve. Fig. S3c and d depicts the CV and GCD curves of Cu_3P@PCNSs-700 sample, consistent with those of Cu_3P@PCNSs-600 sample carbonized at 600℃. According to the Fig. S3, the lithium storage mechanism of Cu_3P@PCNSs-600 and Cu_3P@PCNSs-700 was similar, primarily relying on the conversion reaction between Cu_3P and Li for reversible lithium storage. However, at the carbonization temperature of 500℃, the CV and GCD curves of Cu_3P@PCNSs-500 samples were different from the other two, and no sifnificant redox peak was observed during the scanning process. According to Fig. S3a, a wide cathode peak was found at 0.75 in the cathode scanning of the first ring. Thus, a conclusion was drawn that the SEI film had a sharp cathode peak at nearly 0.2 V, corresponding to the process of lithium embedding in carbon materials. It was therefore revealed that the deembedding

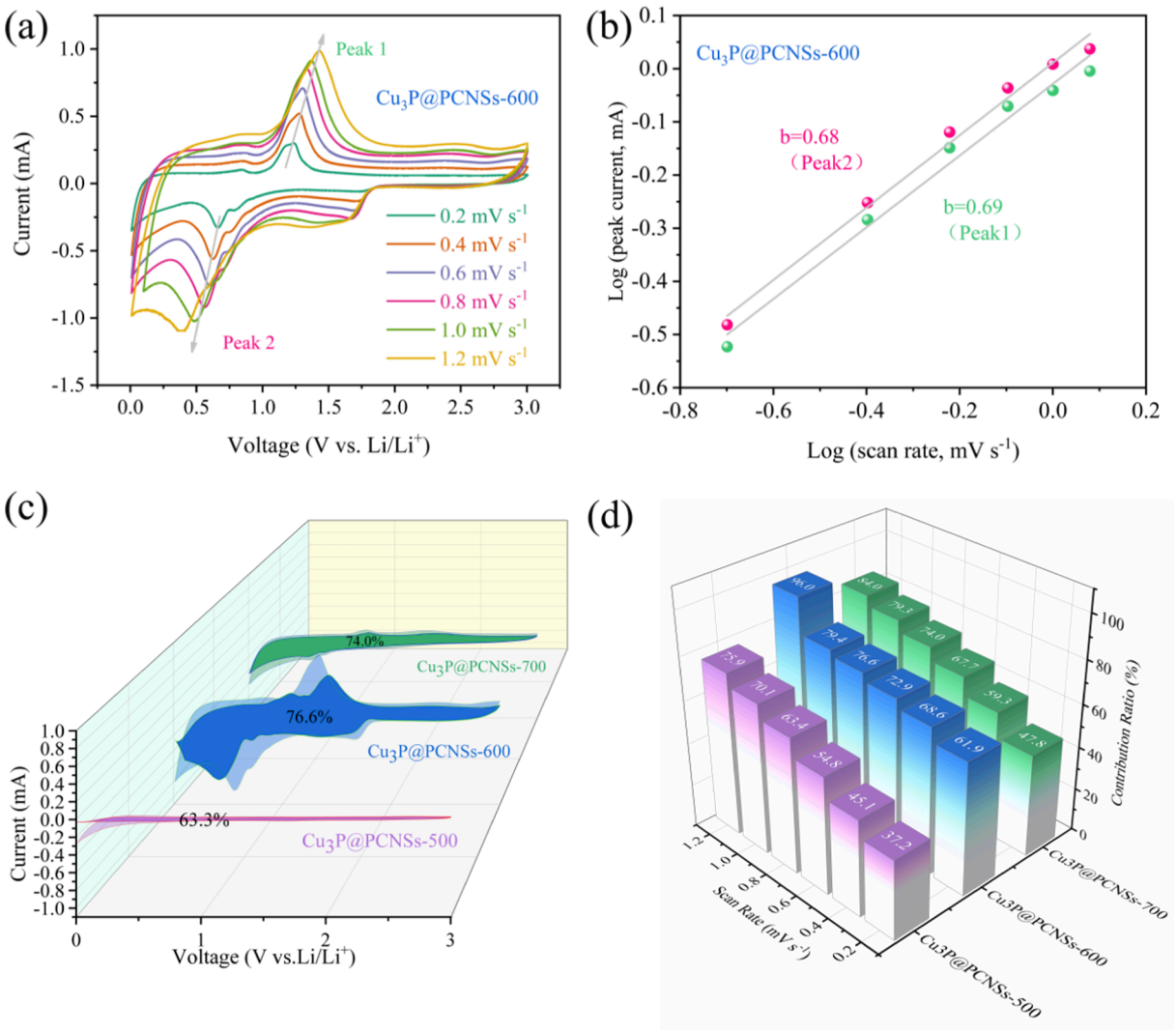

Fig. 5. (a) Cyclic voltammetry of Cu_3P@PCNSs-600 electrode materials at different speeds; (b) logarithmic relationship between peak current and sweep speed of Cu_3P@PCNSs-600 electrode material; (c-d) contribution of pseudocapacitance at different scanning rates for Cu_3P@PCNSs-500, Cu_3P@PCNSs-600 and Cu_3P@PCNSs-700 samples.

mechanism of Cu_3P@PCNSs-500 samples was similar to that of carbon materials, and the deembedding/lithium process of carbon was dominant.

Fig. 4d compares the charge and discharge specific capacities of the first ring of the four samples at the current density of 0.1 A g^{-1}, and the values are presented below: Cu_3P@PCNSs-500 (217.7/1407.6 mA h g^{-1}), Cu_3P@PCNSs-600 (738.9/1292.6 mA h g^{-1}), Cu_3P@PCNSs-700 (567.8/1149.2 mA h g^{-1}) and Cu_3P (393.9/429.9 mA h g^{-1}). The first Coulombic efficiencies of the four samples were calculated as 15.46 %, 57.16 %, 49.41 % and 84.65 %. The specific capacity of the unrecovered part was attributed to irreversible specific capacity and capacity loss caused by SEI film formation. From the numerical perspective, the irreversible capacity loss of Cu_3P@PCNSs-500 sample was the largest and the efficiency was the lowest, probably due to caused by the generation of more SEI caused by the carbon lithium storage mechanism. Cu_3P@PCNSs-600 samples were characterized by large initial charge–discharge capacity and appropriate initial efficiency. Fig. 4e compares the comparison of the rate performance of Cu_3P@PCNSs-500, Cu_3P@PCNSs-600, Cu_3P@PCNSs-700 and Cu_3P samples. When the current densities are 0.1, 0.2, 0.5, 0.8, 1.0 and 2.0 A g^{-1} respectively, the discharge specific capacities of Cu_3P@PCNSs-600 are 1292.6, 592.3, 526.2, 472.1, 437.9 and 383.4 mA h g^{-1}, respectively. When the current density returned to 0.1 A g^{-1}, Cu_3P@PCNSs-600 also recovered to 706.8 mA h g^{-1} and gradually stabilized in subsequent charge–discharge cycles. Moreover, it can be clearly observed from the Fig. 4e that the reversible specific capacity of Cu_3P@PCNSs-600 electrode is larger than that of Cu_3P@PCNSs-500 and Cu_3P@PCNSs-700 at each current density. The above shows that the Cu_3P@PCNSs-600 has the best rate performance when the carbonization temperature is 600℃. Fig. 4f illustrates the cyclic performance of the three samples. Cu_3P@PCNSs-600 had the optimal cycling performance at the current density of 0.5 A g^{-1}. According to the above figure, the capacity of the three 2D doped carbon coated Cu_3P samples increased during the cycling process, which arose from attributed the gradual activation of electrode materials. The capacity of the three 2D-doped carbon-coated Cu_3P samples all increased during cycling, which is attributed to the following two factors: (1) the three electrode materials are of a highly mesoporous structure, which could facilitate the infiltration of electrolyte and contributes to the activation of electrode material; (2) Phosphorus-doped nanosheets could provide more active sites for Li storage [44,45]. Fig. 4g presents the long cycle performance of $1A^{-1}$ at large current. After 1000 cycles, the specific capacity of Cu_3P@PCNSs-600 could still reach 400 mA h g^{-1}.

To gain more insights into the properties of the charge storage mechanism of Cu_3P@PCNSs, the electrochemical kinetic behavior of Cu_3P@PCNSs was investigated at small scanning rates. The specific

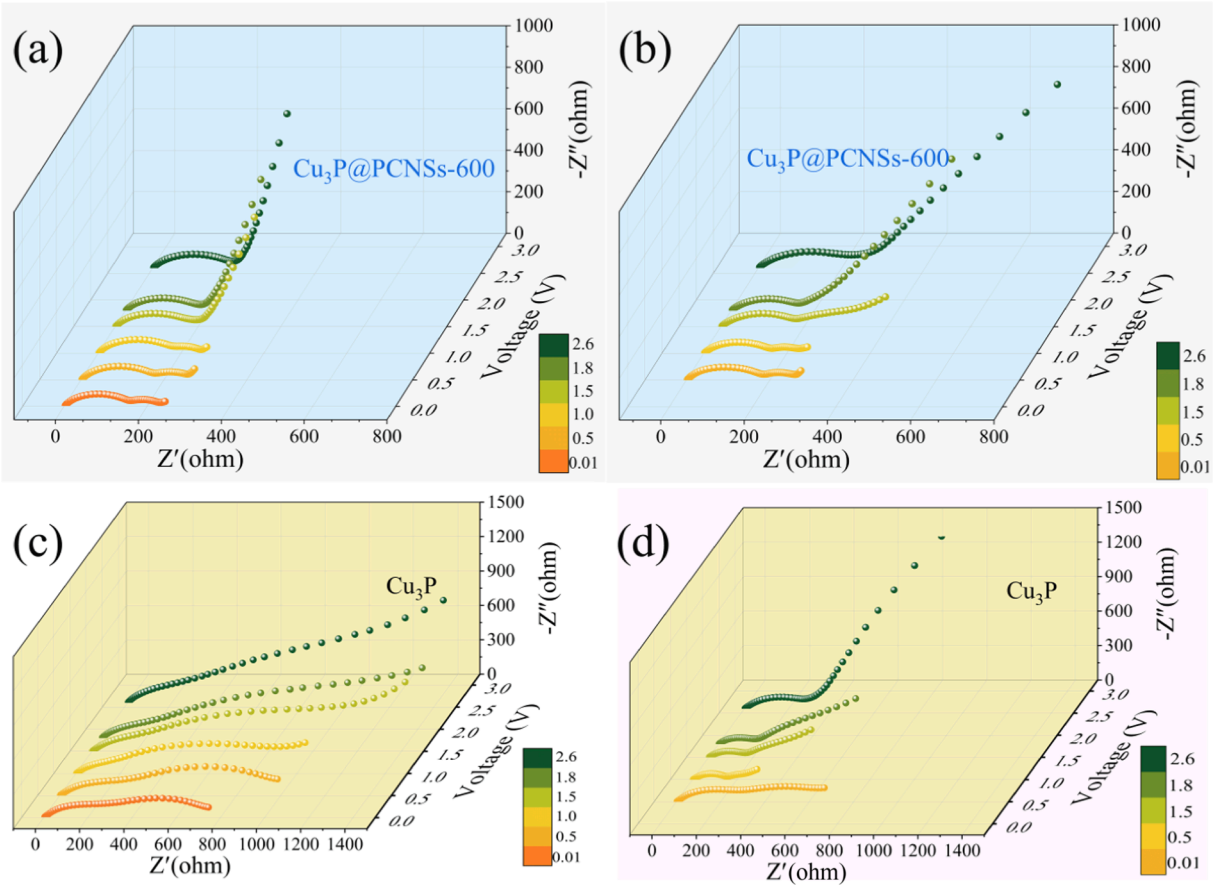

Fig. 6. (a-b) Nyquist plots of the electrodes made of Cu_3P@PCNSs-600 in the first lithium implantation (discharge) and delithium (charge) states; (c-d) Nyquist plots of Cu_3P electrodes in the first lithium implanted and delithium state.

methods are presented below:

In CV test, for electrode materials, the value of b was calculated by Equation (1) to determine whether there is pseudocapacitance behavior in the charging and discharging processes [46].

$$i = av^b \tag{1}$$

where i denotes the peak current response (unit: mA); V represents the sweep speed (mV s^{-1}); A and b are constants. In the case of battery behavior, the peak current i changed with the power 0.5 of the sweep voltage v, i.e., the process was diffusion controlled. If it was pseudocapacitance behavior, the peak current i changed linearly with the scanning voltage v, i.e., the process was capacitive control. When b ranged from between 0.5 and 1, both factors could have contribution [47].

Equation (2) can be obtained by taking logarithms of both sides of Equation (3.1):

$$logi = blogv + loga \tag{2}$$

To further quantify the proportion of the two control processes in the material capacity, Fig. 5a shows the CV curves of Cu_3P@PCNSs-600 at 0.2, 0.4, 0.6, 0.8, 1.0, and 1.2 mV·s^{-1}. With the increase of scanning speed, each CV shows similar shape. In order to explain the storage mechanism of surface compatibility and diffusion control contribution, Dunn method was adopted to calculate and estimate b value, and the calculation results are presented in Fig. 5b. The value of Cu_3P@PCNSs-600 negative electrode b was obtained as 0.68 and 0.69, which could be the common control process of capacitance and diffusion. It was confirmed that the material has a certain capacitance behavior.

To further determine contribution rate of pseudocapacitance behavior and diffusion behavior to charge storage, Equation (1) can be adopted to calculate contribution rate of pseudocapacitance at a specific sweep speed by Equation (3):

$$i(V) = K_1 v + K_2 v^{\frac{1}{2}} \tag{3}$$

where $K_1 v$ and $K_2 v^{\frac{1}{2}}$ represent the response of pseudocapacitance and battery reaction, respectively. Eq. (3.3) can be transformed into Equation (4):

$$i(V)/v^{\frac{1}{2}} = K_1 v^{\frac{1}{2}} + K_2 \tag{4}$$

where denotes the current under a specific voltage; v denotes the sweep speed under a specific voltage; v expresses the specified voltage; K_1 and K_2 are adjustable parameters, and the value of K_1 was obtained through linear fitting of $i(V)/v^{\frac{1}{2}}$ and $v^{\frac{1}{2}}$ in Equation (3). To compare the effect of different treatment temperatures on the lithium storage kinetics of electrode materials, the CV curves of Cu_3P@PCNSs-500 and Cu_3P@PCNSs-700 electrodes at different scanning speeds were simultaneously tasted at the carbonization temperatures of 500℃and 700℃, and the b valuem was calculated, as jpresented in Fig. S4. Furthermore, the pseudocapacitance contribution rate at 1MVS-1was compared (Fig. 5c). According to the Fig. 5, Cu_3P@PCNSs-600 electrode material has the largest capacitance contribution rate. In addition,as indicated by Fig. 5d, the contribution of pseudocapacitance tended to increase with the increase in the scanning speed. When the scanning rate increased from 0.2 mV·s^{-1} to 1.2 mV·s^{-1}, the contribution rate was elevated from 61.9 % to 96.0 %. As revealed by the above results, the charge storage process of Cu_3P@PCNSs-600 was dominated by capacitance and showed good dynamic behavior.

Fig. 6 presents the Nyquist diagram of Cu_3P@PCNSs-600 and Cu_3P

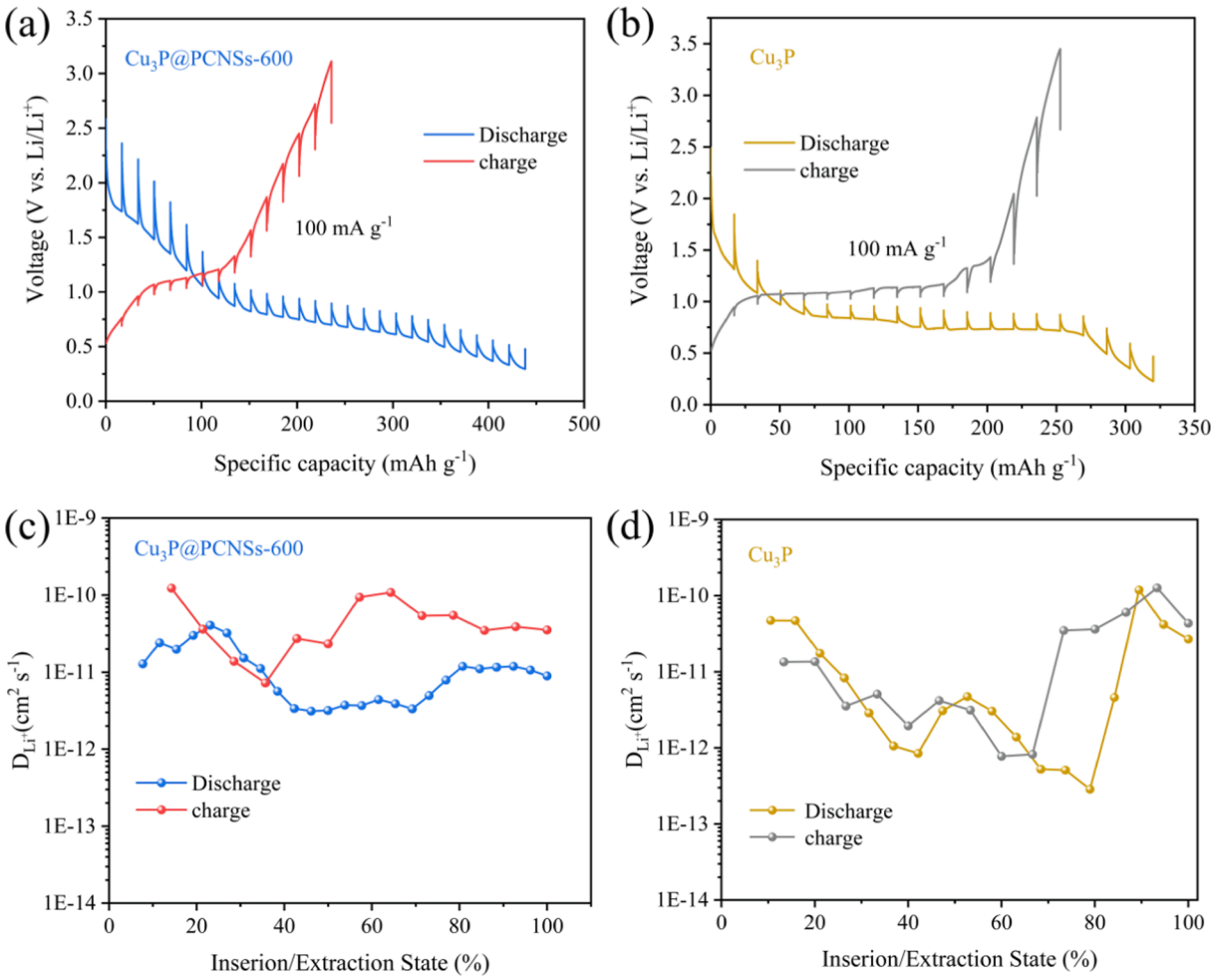

Fig. 7. (a) GITT curve of Cu_3P@PCNSs-600 electrode; (b) GITT curve of Cu_3P electrode; (c) Calculate the Li^+ diffusion system of Cu_3P@PCNSs-600 (c) and the original Cu_3P electrode (d) in different charge and discharge states.

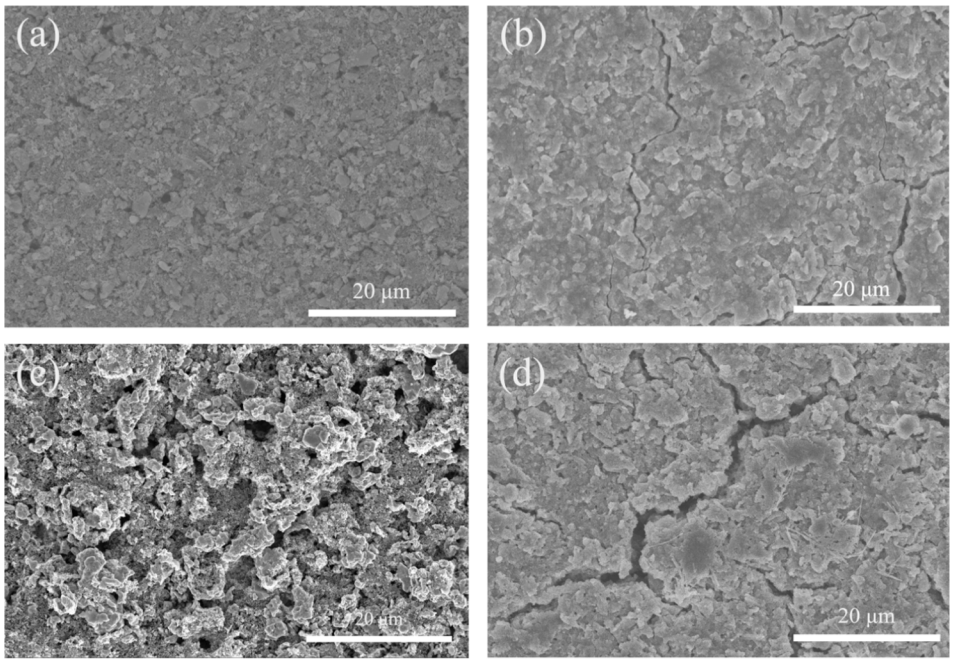

Fig. 8. SEM images of (a) Cu_3P@PCNSs-600 and (c) pure Cu_3P electrode before cycling; SEM images of (b) Cu_3P@PCNSs-600electrode and (d) pure Cu_3P electrode after 200 cycles at 0.5 A g^{-1}.

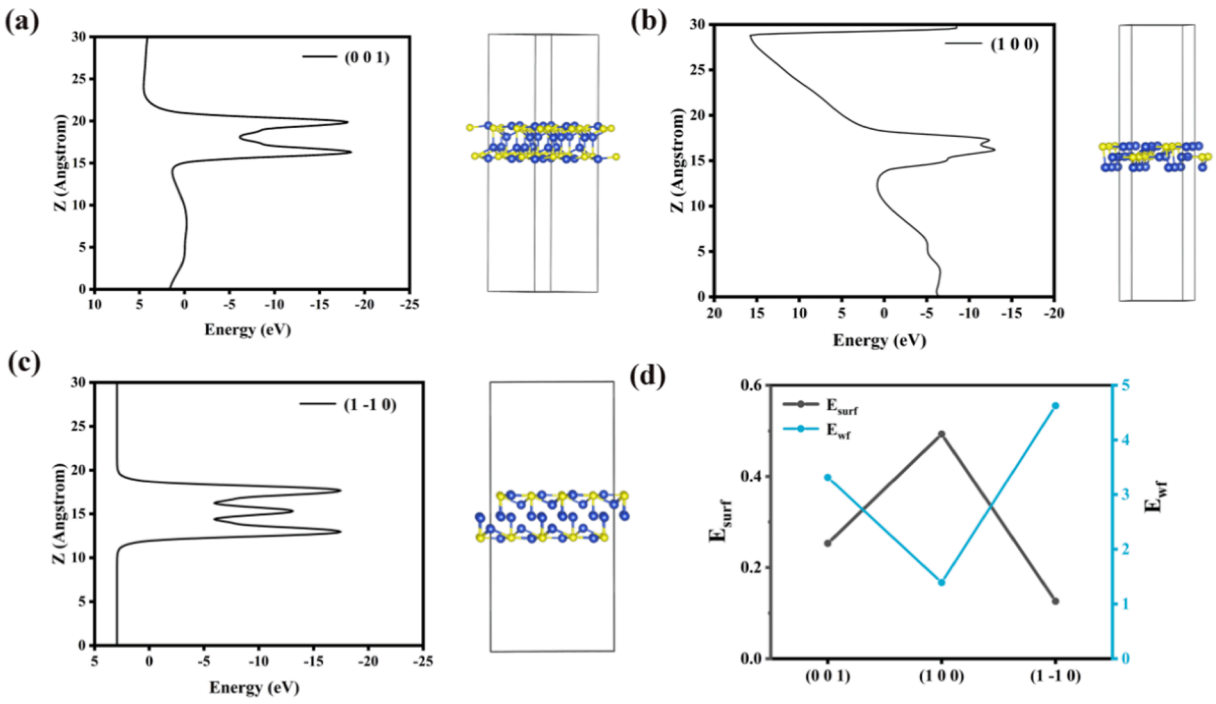

Fig. 9. (a-c) Surface work function images of crystal planes of Cu_3P (0,0,1), (1,0,0) and (1,-1,0); (d) Surface work functions and surface energies of Cu_3P (0,0,1), (1,0,0) and (1,-1,0).

electrodes under the charging conditions of different discharge charges in the first cycle. According to Fig. 6a and b, the first charge and discharge out-of-situ EIS test results indicated that the battery's Rs remained at 1.5–2 Ω without significant change. The Rct decreased, then increased, and lastly decreased. The initial increase might arise from the formation of the intermediate $Li_XCu_{3-X}P$ in Cu_3P transformation reaction, while the rise of the intermediate stage was owing to the effect of SEI membrane. At the subsequently stage, the Rct decreased due to the increase of metal Cu and the shrinkage of the structure. During the discharge process, the Nyquist diagram changed with the increase in the potential, and it showed a reversible behavior with the decrease in the potential. In Fig. 6c and d, when the Cu_3P electrode discharge was lower than 0.5 V, the mid-frequency semicircle decreased significantly. With the continuouse charging process, mid-frequency semicircle tended to increase. However, for Cu_3P@PCNSs-600 electrode, the mid-frequency semicircle appeared at about 1.0 V, corresponding to the generation of SEI film, and the mid-frequency semicircle was relatively stable in the charging and discharging procedures, and there was no significant change.

To fully understand the diffusion kinetics of the electrode material, the diffusion coefficient D of Li^+ in the electrode was determined by constant current intermittent titration[48]. Fig. 7a and b present the GITT curves of Cu_3P@PCNSs-600 electrode and original Cu_3P electrode respectively. The GITT curves were well consistent with the volt-capacity curves previously tested. Using GITT data, the diffusion coefficients of lithium ions in Cu_3P@PCNSs-600 electrode and original Cu_3P electrode at different discharge voltages can be determined as Equation (5) [49]:

$$D_{Li} = \frac{4}{\pi\tau}\left(\frac{m_B V_m}{M_B A}\right)^2\left(\frac{\Delta E_s}{\Delta E_\tau}\right)^2 \left(\tau \ll L^2/D_{Li}\right) \quad (5)$$

where V_m denotes the molar volume; M_B and m_B represent the molecular weight of the material and the mass of the active substance, respectively; A expresses the surface area of the electrode; L is the thickness of the electrode, ΔE_s and ΔE_τ are the voltage change after the current flux and the open state and the voltage change during the constant current pulse process respectively. Fig. 7(c-d) presents the diffusion coefficient of lithium ions in Cu_3P@PCNSs-600 electrode and original Cu_3P electrode. It was clearly indicated from the Fig. 7 that the diffusion coefficient of Cu_3P@PCNSs-600 electrode was greater than that of original Cu_3P, indicating that the composite material significantly reduceds the contact resistance of the electrode and increased the diffusion rate of lithium ions.

In order to further determine the stability of the electrode after cycling, we investigated the change in the morphology of of pure Cu_3P and Cu_3P@PCNSs-600 electrodes after charging and discharging. Fig. 8a and b show the surface states of Cu_3P@PCNSs-600 and pure Cu_3P before circulation respectively. It can be seen that Cu_3P@PCNSs-600 is evenly dispersed and has a dense surface after coating. However, the pure Cu_3P electrodes presents a large number of spherical particles with sparse and loose surface, which is not conducive to electron conduction. After the cycle, due to the expansion and contraction of uncoated Cu_3P particles in the charging and discharging process, obvious cracks appeared on the electrode surface. However, under the stable carbon coating, the Cu_3P@PCNSs-600 electrode (Fig. 8b) basically maintained its original shape after 200 cycles, without obvious morphological damage. the 2D structure of Cu_3P@PCNSs-600 effectively buffered the volume change of Cu_3P nanoparticles and inhibited the electrode cracking during the cycling process.

3.3. Density functional theory (DFT) calculations

DFT calculation was conducted to further study the mechanism of the electrochemical performance difference between Cu_3P@PC and Cu_3P. To analyze the adsorption on solid surface, the basic properties exhibited by the surface should be understood (e.g., surface energy and surface work function). In this studty, the growth morphology of Cu_3P was predicted using morphological prediction method Bravais-Friedel-Donnay-Harker (BFDH) [50,51] in commercial software Materials Studio. In existing studies, BFDH was adopted to successfully predict the optimal surface of Co_2O [52]. According to the Fig. S5, as indicated by the output results of BFDH calculation, the exposed surface of Cu_3P structure might have (0,0,1), (1,0,0) and (1,-1,0) crystal faces (denoted

Table 1
Li^+ adsorption site, Li adsorption energy of Cu_3P and Cu3P@PCNSs.

Structure	Site	E_{ad} (eV)
Cu_3P	H	−2.79167702
	B	−2.09236983
	T	−1.22589586
Cu3P@PCNSs	H	−3.57096166
	B	−2.26124540
	T	−2.18314399

by $surf_1$, $surf_2$ and $surf_3$, respectively). After the above three surfaces were determined as research objects, the most stable surface structure was determined by calculating the surface energy and surface work function of the three truncated surfaces [53]. Surface energy has been found as a vital index to measure surface stability, which can be expressed by Equation (6) [54]:

$$E_{surf} = \frac{1}{2A}(E_{slab} - nE_{bulk}) \tag{6}$$

where n represents the number of atoms contained in Slab; E_{slab} denotes the total energy of the selected Slab model; E_{bulk} express the energy of each proto-cell; A refers to the surface area of crystal cell. Fig. 9 presents the calculation results of surface energy. The larger the surface energy is, the more unstable the Slab model would be. The surface work function is the minimum energy required for electrons to move from the interior of a solid to the surface, which can be determined by Equation (7) [55]:

$$E_{wf} = E_{vacuum} - E_{fermi} \tag{7}$$

where E_{vacuum} denotes the electrostatic potential energy at the vacuum away from the surface; E_{fermi} represents the electrostatic potential energy

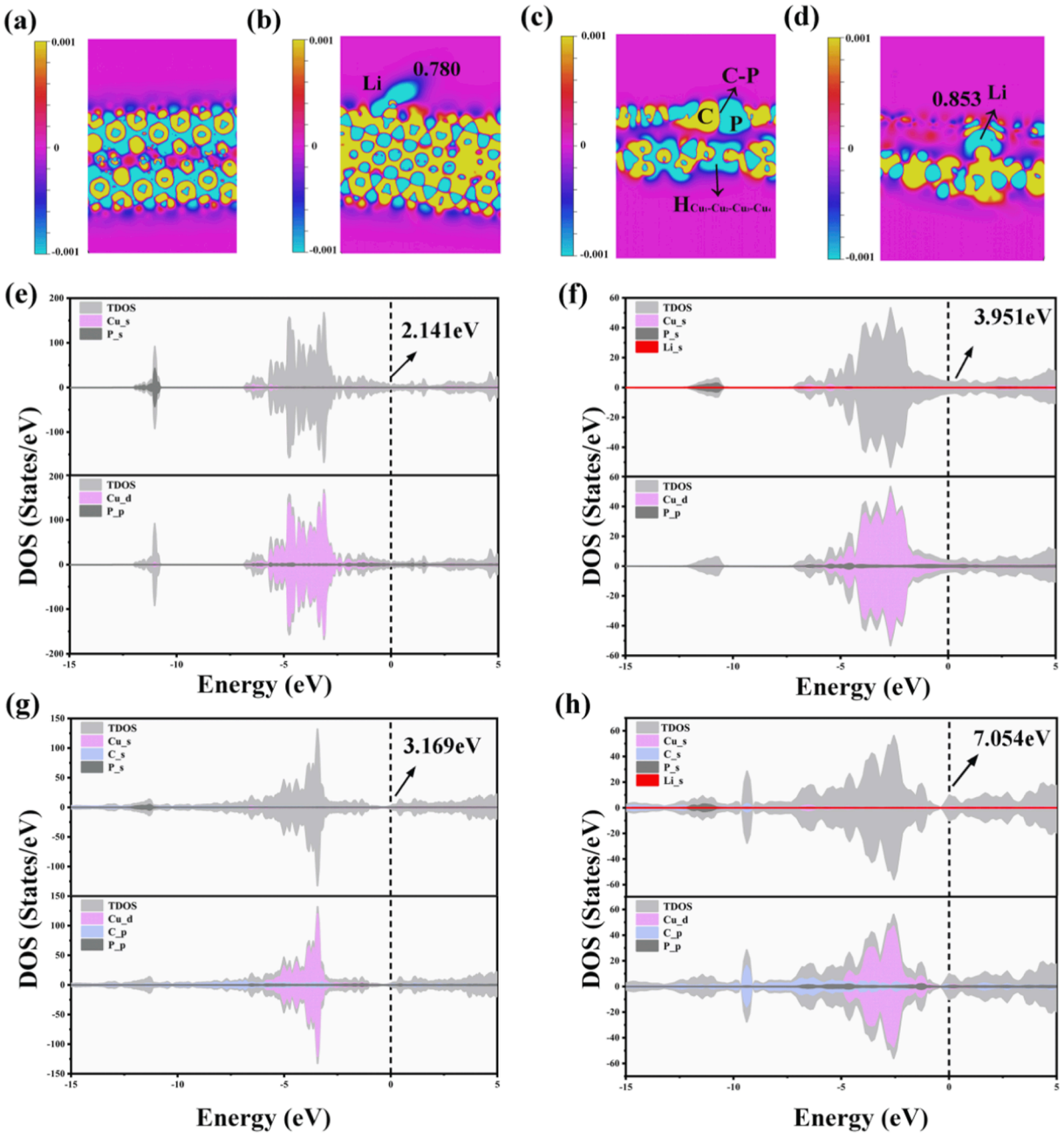

Fig. 10. Charge distribution on (a) Cu_3P and (c) Cu_3P@PCNSs; 2D charge density difference plots of Li adsorption on (b) Cu_3P and (d) Cu_3P@PCNSs; PDOS (before adsorption) of the (e) Cu_3P and (g) Cu_3P@PCNSs; PDOS (after adsorption) of the (f) Cu_3P and (h) Cu_3P@PCNSs;

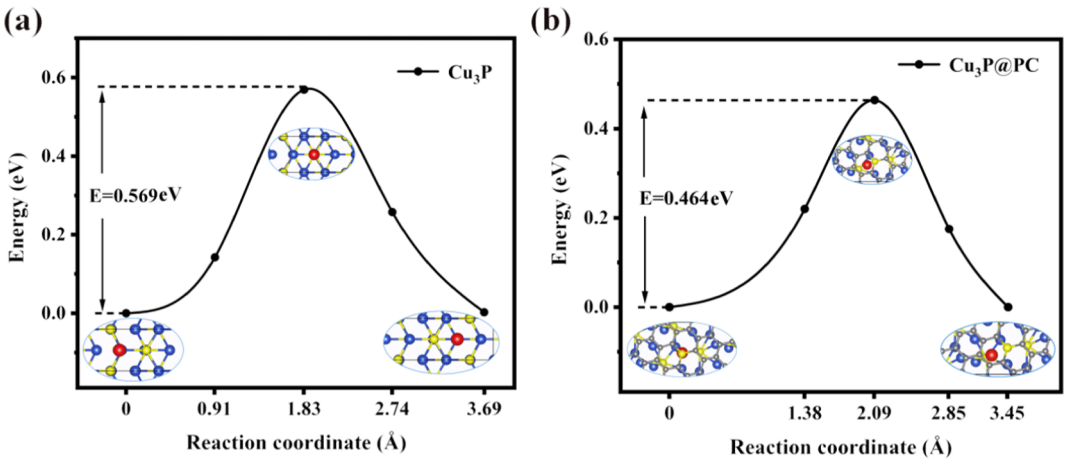

Fig. 11. The diffusion barrier of Li on (a) Cu_3P and (b) Cu_3P@PCNSs.

at the Fermi level. According to the Fig. 9, the electrostatic potential energy in the vacuum region was shown as a straight line, which indicated that the potential function converged in the vacuum region. The electrostatic potential energy between atomic layers showed a curve of oscillation, and the intensity of oscillation between atomic layers was in order, thus indicating that the interaction between atoms on the (-1,1,0) plane was the largest, consistent with the calculation result of surface energy. In brief, (-1,1,0) represents the most likely exposed and most suitable crystal plane for lithium atom adsorption.

The heterogeneous structure Cu_3P@PCNSs was built with using Cu_3P (-1,1,0) crystal plane and carbon matrix model as the initial model using vaspkit module in VASP software, and the structure was improved as presented in the Fig. S6. Using VASP software to build heterogeneous structures has formed a very mature computing system [56], which can accurately set the lattice compatibility and vacuum layer thickness. It is helpful to reduce lattice fit and subsequent adsorption behavior calculation. Based on existing studies, graphene was used instead for the carbon matrix model in our calculations [57]. Subsequently, the lithium storage capacity of Cu_3P and Cu_3P@PCNSs was investigated by calculating the adsorption energy of a single lithium atom [58]. The adsorption structures of different adsorption sites are shown in Fig. S7. Table1 lists the specific adsorption sites and calculation results. As indicated by the calculation results, the adsorption energy of Li on Cu_3P@PCNSs structure was significantly greater than that of Cu_3P, consistent with the results of previous experiments.

As reported by existing studies, the difference in electrostatic attraction between the transition metal phosphating surface and the graphene plane can have significant effect on the adsorption behavior of Li^+. Accordingly, differential charges of the two structures were calculated, and the differential charge diagram were drawn to measure the synergistic effect arising from the heterogeneous structures. According to the Fig. 10a-d, the blue area represents a decrease in the charge density, and the yellow area represents an increase in the charge density. When Li ions were inserted into the inner layer of Cu_3P@PCNSs, the absorbed Li largely interacted with the carbon matrix layer on the surface, and the charge lost by Li was transferred to the adjacent PC surface to form an ionic bond. Moreover, the transfer charge was studied through Bader charge study [59]. As revealed by the calculation results, the transfer charge of Li adsorbed on Cu_3P@PCNSs was 0.853 (Fig. 10d), and the transfer charge of Li adsorbed on Cu_3P was 0.780 (Fig. 10b), thus confirming that there was a more significant interaction between Li and the hetero structure, which could help increase the electronic conductivity of the anode.

To acquire more understanding into the adsorption mechanism of Li^+ on the heterogeneous structure, the state densities of the two structures were calculated. According to Fig. 10e and g, the state densities of Cu_3P and Cu_3P@PCNSs at the Fermi level were 2.141 eV and 3.169 eV, respectively. The state density of Cu_3P@PCNSs at the Fermi level was significantly larger than that of Cu_3P, which confirmed that the electronic conductivity of the structure could be improved by combining carbon matrix with Cu_3P. The conduction bands of Cu_3P and Cu_3P@PCNSs were primarily occupied by Cu 3d orbitals, and the valence bands generally consisted of P 3p orbitals and C 2p orbitals. After Li atom was adsorbed, the densities of DOS at the Fermi level of Cu_3P and Cu_3P@PCNSs were 3.951 eV and 7.054 eV (Fig. 10f and h), respectively, significantly higher than those without the adsorption of Li, which revealed that the densities of states near the Fermi level played a vital role in the chemical activity of the structure. When the adsorption occurred, the interaction between Li atom and carbon matrix plane took place, thus increasing the energy of the Fermi energy level and improving the electronic conductivity.

The ion diffusion rate determined the fast charge and discharge rate of the material, and it was found as critical performance factor [60]. The diffusion coefficient of metal ions can be obtained by Equation (8) [61]:

$$D = D_0 exp\left(-\frac{\Delta E_b}{kT}\right) \quad (8)$$

where D_0, ΔE_b, k and T are pre-exponential factor, diffusion barrier, Boltzmann constant and absolute temperature, respectively[62]. In this study, the main barrier to overcome for the migration of Li occurred in the vicinity of Cu-P bond and C-C bond. According to Fig. 11, the diffusion barrier of Cu_3P was 0.569 eV, and the recombination of Cu_3P with carbon matrix structure significantly induced the adsorption of Li atom. The above induction effectively reduced the barrier of atomic diffusion(e.g., crossing C-C bond and Cu-P bond). The migration barrier of the diffusion path on Cu_3P@PCNSs structure was optimized (0.464 eV), compliance with the GITT calculation consequences in the experiment. It was therefore, revealed that the heterogeneous structure could favorable to the maintenance of excellent ionic conductivity at the low energy barrier, thus providing an advantage for the excellent diffusion ability of lithium ions.

4. Conclusion

In brief, the ultrafine Cu_3P nanoparticles prepared in this study were well embedded into the phospho-doped carbon nanosheet, which was synthesized from 2D Cu-BDC derived carbon. In the obtained material obtained, Cu_3P nanoparticles were evenly embedded into the carbon matrix, and phosphorus doping increased the active sites for storing Li^+ and improved the electrical conductivity of the material. The porous structure was found to inhibit the agglomeration of Cu_3P nanoparticles in the charging and discharging processes, which ensured the integrity

of the electrode. Because of this reasonable advancement, the Cu_3P@PCNSs-600 composite anode exhibited outstanding rate capability (383.4 mAh g^{-1} at 2 A g^{-1}), outstanding cyclic stability (436.4 mAh g^{-1} at 1 A g^{-1} over 1000 cycles) for lithium storage. As revealed by the results of DFT, the doping effect of P atom was significantly correlated with the difference of atomic radius and electronegativity between P and C atoms. Moreover, the charge transfer and conductive behavior between the heterostructures had an effect on the adsorption capacity of Li^+. Thus, Cu_3P@PCNSs electrode materials were characterized by better rate property and cycle stability. This study presented more insights into the storage mechanism of heterogeneous structure, which is of high significance to the design of excellent transition metal phosphating electrode materials.

Author Contributions.

The manuscript was written through contributions of all authors. All authors have given approval to the final version of the manuscript.

Declaration of Competing Interest

The authors declare that they have no known competing financial interests or personal relationships that could have appeared to influence the work reported in this paper.

Acknowledgements

This research was financially supported by the National Natural Science Foundation of China (No. 51871238 and 52171227), key research and development project of Jiangsu Province BE2021633, the science and technology project of Xuzhou KC21338, the Research Funds for the Central Scientific 2021ZDPY0221, the Postdoctoral Research Funding Program of Jiangsu Province (No.2021K043A)

Appendix A. Supplementary material

Supplementary data to this article can be found online at https://doi.org/10.1016/j.apsusc.2022.153915.

References

[1] Y. Zhang, Z.-F. Wu, P.-F. Gao, S.-L. Zhang, Y.-H. Wen, Could Borophene Be Used as A Promising Anode Material for High-performance, (n.d.) 3.
[2] B. Mortazavi, O. Rahaman, S. Ahzi, T. Rabczuk, Flat borophene films as anode materials for Mg, Na or Li-ion batteries with ultra high capacities: A first-principles study, Appl. Mater. Today 8 (2017) 60–67, https://doi.org/10.1016/j.apmt.2017.04.010.
[3] S. Liu, J. Zhou, H. Song, Tailoring Highly N-Doped Carbon Materials from Hexamine-Based MOFs: Superior Performance and New Insight into the Roles of N Configurations in Na-Ion Storage, Small 14 (12) (2018) 1703548.
[4] J. Han, J. Ren, Optimization of cycling performance of hollow Cu2S@NC cubes anode for lithium-ion batteries in ether-based electrolyte, J. Mater. Sci. 56 (2021) 19119–19127, https://doi.org/10.1007/s10853-021-06437-5.
[5] Y. Liu, B. Jin, Y.F. Zhu, X.Z. Ma, X.Y. Lang, Synthesis of Cu 2 S/carbon composites with improved lithium storage performance, Int. J. Hydrogen Energy 40 (2015) 670–674, https://doi.org/10.1016/j.ijhydene.2014.10.133.
[6] W. Xie, K. Liu, G. Shi, X. Fu, X. Chen, Z. Fan, M. Liu, M. Yuan, M. Wang, CoS2 nanowires supported graphdiyne for highly efficient hydrogen evolution reaction, J. Energy Chem. 60 (2021) 272–278, https://doi.org/10.1016/j.jechem.2021.01.005.
[7] Y. Xie, Y. Wang, Electronic structure and electrochemical performance of CoS2/MoS2 nanosheet composite: Simulation calculation and experimental investigation, Electrochim. Acta. 364 (2020), 137224, https://doi.org/10.1016/j.electacta.2020.137224.
[8] T. Mu, P. Zuo, S. Lou, Q. Pan, H. Zhang, C. Du, Y. Gao, X. Cheng, Y. Ma, H. Huo, G. Yin, A three-dimensional silicon/nitrogen-doped graphitized carbon composite as high-performance anode material for lithium ion batteries, J. Alloy. Compd. 777 (2019) 190–197, https://doi.org/10.1016/j.jallcom.2018.10.177.
[9] T. Mu, P. Zuo, S. Lou, Q. Pan, Q. Li, C. Du, Y. Gao, X. Cheng, Y. Ma, G. Yin, A two-dimensional nitrogen-rich carbon/silicon composite as high performance anode material for lithium ion batteries, Chem. Eng. J. 341 (2018) 37–46, https://doi.org/10.1016/j.cej.2018.02.026.
[10] J. Zhu, Q. He, Y. Liu, J. Key, S. Nie, M. Wu, P.K. Shen, Three-dimensional, heterostructured, Cu_3P@C nanosheets with excellent cycling stability as Na-ion battery anode material, J. Mater. Chem. A. 7 (2019) 16999–17007, https://doi.org/10.1039/C9TA04035H.
[11] H. Pfeiffer, F. Tancret, T. Brousse, Synthesis, characterization and electrochemical properties of copper phosphide (Cu3P) thick films prepared by solid-state reaction at low temperature: a probable anode for lithium ion batteries, Electrochim. Acta. 50 (2005) 4763–4770, https://doi.org/10.1016/j.electacta.2005.02.024.
[12] L. De Trizio, A. Figuerola, L. Manna, A. Genovese, C. George, R. Brescia, Z. Saghi, R. Simonutti, M. Van Huis, A. Falqui, Size-Tunable, Hexagonal Plate-like Cu_3P and Janus-like Cu–Cu_3P Nanocrystals, ACS Nano 6 (2012) 32–41, https://doi.org/10.1021/nn203702r.
[13] Y. Yun, B. Xi, Y. Gu, F. Tian, W. Chen, J. Feng, Y. Qian, S. Xiong, Cu3P nanoparticles confined in nitrogen/phosphorus dual-doped porous carbon nanosheets for efficient potassium storage, J. Energy Chem. 66 (2022) 339–347, https://doi.org/10.1016/j.jechem.2021.05.045.
[14] J. Tian, Q. Liu, N. Cheng, A.M. Asiri, X. Sun, Self-Supported Cu_3P Nanowire Arrays as an Integrated High-Performance Three-Dimensional Cathode for Generating Hydrogen from Water, Angew. Chem. Int. Ed. 53 (2014) 9577–9581, https://doi.org/10.1002/anie.201403842.
[15] X. Wang, Q. Pan, Y. Xie, L. Wang, J. Liu, S. Wang, K. Pan, Monodisperse Cu3P nanoplates in situ grown on reduced graphene oxide via hydrophobic interaction for water splitting, Mater. Lett. 306 (2022), 130947, https://doi.org/10.1016/j.matlet.2021.130947.
[16] Q. Feng, T. Li, Y. Miao, Y. Sui, B. Xiao, Z. Sun, J. Qi, F. Wei, Q. Meng, Y. Ren, X. Xue, Polyvinylpyrrolidone assisted transformation of Cu-MOF into N/P-co-doped Octahedron carbon encapsulated Cu3P nanoparticles as high performance anode for lithium ion batteries, J. Colloid Interface Sci. 608 (2022) 227–238, https://doi.org/10.1016/j.jcis.2021.09.147.
[17] Y. Liu, L. Wu, Q. Liu, L. Liu, S. Ke, Z. Peng, T. Shi, X. Yuan, H. Huang, J. Li, C. Ye, P. K. Chu, J. Wang, X.-F. Yu, Topochemical Synthesis of Copper Phosphide Nanoribbons for Flexible Optoelectronic Memristors, Adv. Funct. Mater. 32 (14) (2022) 2110900.
[18] S. Liu, X. He, J. Zhu, L. Xu, J. Tong, Cu3P/RGO Nanocomposite as a New Anode for Lithium-Ion Batteries, Sci. Rep. 6 (2016) 35189, https://doi.org/10.1038/srep35189.
[19] R. Wei, M. Huang, W. Ma, B. Xi, Z. Feng, H. Li, J. Feng, S. Xiong, N-doped carbon nanotubes formed in a wide range of temperature and ramping rate for fast sodium storage, J. Energy Chem. 49 (2020) 136–146, https://doi.org/10.1016/j.jechem.2020.01.010.
[20] C. Guo, W. Zhang, Y. Liu, J. He, S. Yang, M. Liu, Q. Wang, Z. Guo, Constructing CoO/Co3S4 Heterostructures Embedded in N-doped Carbon Frameworks for High-Performance Sodium-Ion Batteries, Adv. Funct. Mater. 29 (2019) 1901925, https://doi.org/10.1002/adfm.201901925.
[21] X. Ou, L. Cao, X. Liang, F. Zheng, H.-S. Zheng, X. Yang, J.-H. Wang, C. Yang, M. Liu, Fabrication of SnS2/Mn2SnS4/Carbon Heterostructures for Sodium-Ion Batteries with High Initial Coulombic Efficiency and Cycling Stability, ACS Nano 13 (2019) 3666–3676, https://doi.org/10.1021/acsnano.9b00375.
[22] L. Mo, X. Xu, Z. Liu, H. Liu, B. Lei, J. Zhuang, Z. Guo, Y. Liu, C. Hu, Visible-light excitable thermally activated delayed fluorescence in aqueous solution from F N-doped carbon dots confined in silica nanoparticles, Chem. Eng. J. 426 (2021), 130728, https://doi.org/10.1016/j.cej.2021.130728.
[23] R. Wang, X.-Y. Dong, J. Du, J.-Y. Zhao, S.-Q. Zang, MOF-Derived Bifunctional Cu_3P Nanoparticles Coated by a N, P-Codoped Carbon Shell for Hydrogen Evolution and Oxygen Reduction, Adv. Mater. 30 (2018) 1703711, https://doi.org/10.1002/adma.201703711.
[24] P. Wang, M. Shen, H. Zhou, C. Meng, A. Yuan, MOF-Derived CuS@Cu-BTC Composites as High-Performance Anodes for Lithium-Ion Batteries, Small. 15 (2019) 1903522, https://doi.org/10.1002/smll.201903522.
[25] X. Liu, F. Liu, X. Zhao, L.-Z. Fan, Constructing MOF-derived CoP-NC@MXene sandwich-like composite by in-situ intercalation for enhanced lithium and sodium storage, J. Materiom. 8 (2022) 30–37, https://doi.org/10.1016/j.jmat.2021.06.002.
[26] Y. Tang, H. Kang, J. Zheng, H. Li, R. Wang, L. Zhang, Q. Ma, X. Xiong, T. Zhou, C. Zhang, Metal-Organic Framework derived Bi2S3 hybrid nanofibers for enhanced lithium-ion storage, J. Power Sources 520 (2022), 230895, https://doi.org/10.1016/j.jpowsour.2021.230895.
[27] N. Li, Y. Li, Q. Li, Y. Zhao, C.-S. Liu, H. Pang, NiO nanoparticles decorated hexagonal Nickel-based metal-organic framework: Self-template synthesis and its application in electrochemical energy storage, J. Colloid Interface Sci. 581 (2021) 709–718, https://doi.org/10.1016/j.jcis.2020.07.134.
[28] J. Yu, T. Sun, Q. Yang, J. Ma, Porous carbon networks containing Si and SnO2 as high performance anode materials for lithium-ion batteries, Mater. Lett. 184 (2016) 169–172, https://doi.org/10.1016/j.matlet.2016.08.047.
[29] P. Xu, K. Dai, C. Yang, X. Wang, R. Zou, J. Shao, G. Zeng, M. Zhang, Q. Huang, Z. Su, Efficient synthesis of Cu3P nanoparticles confined in 3D nitrogen-doped carbon networks as high performance anode for lithium/sodium-ion batteries, J. Alloy. Compd. 849 (2020), 156436, https://doi.org/10.1016/j.jallcom.2020.156436.
[30] L. Grajciar, O. Bludský, P. Nachtigall, Water Adsorption on Coordinatively Unsaturated Sites in CuBTC MOF, J. Phys. Chem. Lett. 1 (2010) 3354–3359, https://doi.org/10.1021/jz101378z.
[31] G. Kresse, J. Hafner, *Ab initio* molecular dynamics for liquid metals, Phys. Rev. B. 47 (1993) 558–561, https://doi.org/10.1103/PhysRevB.47.558.
[32] G. Kresse, J. Hafner, *Ab initio* molecular-dynamics simulation of the liquid-metal–amorphous-semiconductor transition in germanium, Phys. Rev. B. 49 (1994) 14251–14269, https://doi.org/10.1103/PhysRevB.49.14251.
[33] G. Kresse, D. Joubert, From ultrasoft pseudopotentials to the projector augmented-wave method, Phys. Rev. B. 59 (1999) 1758–1775, https://doi.org/10.1103/PhysRevB.59.1758.

[34] P.E. Blöchl, Projector augmented-wave method, Phys. Rev. B. 50 (1994) 17953–17979, https://doi.org/10.1103/PhysRevB.50.17953.
[35] J.P. Perdew, K. Burke, M. Ernzerhof, Generalized Gradient Approximation Made Simple, Phys. Rev. Lett. 77 (1996) 3865–3868, https://doi.org/10.1103/PhysRevLett.77.3865.
[36] S. Grimme, Semiempirical GGA-type density functional constructed with a long-range dispersion correction, J. Comput. Chem. 27 (2006) 1787–1799, https://doi.org/10.1002/jcc.20495.
[37] V.N. Jafarova, G.S. Orudzhev, Structural and electronic properties of ZnO: A first-principles density-functional theory study within LDA(GGA) and LDA(GGA)+U methods, Solid State Commun. 325 (2021), 114166, https://doi.org/10.1016/j.ssc.2020.114166.
[38] Q. Meng, T. Wang, E. Liu, X. Ma, Q. Ge, J. Gong, Understanding electronic and optical properties of anatase TiO2 photocatalysts co-doped with nitrogen and transition metals, Phys. Chem. Chem. Phys. 15 (2013) 9549, https://doi.org/10.1039/c3cp51476e.
[39] Q. Feng, T. Li, Y. Sui, B. Xiao, T. Wang, Z. Sun, J. Qi, F. Wei, Q. Meng, Y. Ren, X. Xue, Facile synthesis and first-principles study of nitrogen and sulfur dual-doped porous graphene aerogels/natural graphite as anode materials for Li-ion batteries, J. Alloy. Compd. 884 (2021), 160923, https://doi.org/10.1016/j.jallcom.2021.160923.
[40] C.-H. Jo, J.H. Jo, J.U. Choi, H. Yashiro, H. Kim, S.-T. Myung, Oxalate-Based High-Capacity Conversion Anode for Potassium Storage, ACS Sustain. Chem. Eng. 8 (2020) 3743–3750, https://doi.org/10.1021/acssuschemeng.9b06951.
[41] T. Liang, S. Lenus, Y. Liu, Y. Chen, T. Sakthivel, F. Chen, F. Ma, Z. Dai, Interface and M^{3+}/M^{2+} Valence Dual-Engineering on Nickel Cobalt Sulfoselenide/Black Phosphorus Heterostructure for Efficient Water Splitting Electrocatalysis, Energy Environ. Mater. (2022) eem2.12332, https://doi.org/10.1002/eem2.12332.
[42] Y. Cui, W. Liu, X. Wang, J. Li, Y. Zhang, Y. Du, S. Liu, H. Wang, W. Feng, M. Chen, Bioinspired Mineralization under Freezing Conditions: An Approach to Fabricate Porous Carbons with Complicated Architecture and Superior K^{+} Storage Performance, ACS Nano 13 (2019) 11582–11592, https://doi.org/10.1021/acsnano.9b05284.
[43] R. Wang, Y. Sui, S. Huang, Y. Pu, P. Cao, High-performance flexible all-solid-state asymmetric supercapacitors from nanostructured electrodes prepared by oxidation-assisted dealloying protocol, Chem. Eng. J. 331 (2018) 527–535, https://doi.org/10.1016/j.cej.2017.09.004.
[44] G. Hu, Z. Gan, Y. Cao, K. Du, Y. Du, Z. Peng, A three-dimensional LiVPO4F@C/MWCNTs/rGO composite with enhanced performance for high rate Li-ion batteries, Electrochim. Acta. 292 (2018) 502–510, https://doi.org/10.1016/j.electacta.2018.09.142.
[45] G.S. Sim, P. Santhoshkumar, J.W. Park, C.W. Ho, N. Shaji, H.K. Kim, M. Nanthagopal, C.W. Lee, Chitosan-derived nitrogen-doped carbon on Li2ZnTi3O8/TiO2 composite as an anode material for lithium-ion batteries, Ceram. Int. 47 (2021) 33554–33562, https://doi.org/10.1016/j.ceramint.2021.08.264.
[46] J. Chu, Q. Yu, K. Han, L. Xing, Y. Bao, W. (Alex) Wang, A novel graphene-wrapped corals-like NiSe2 for ultrahigh-capacity potassium ion storage, Carbon. 161 (2020) 834–841. https://doi.org/10.1016/j.carbon.2020.02.020.
[47] M. Park, X. Zhang, M. Chung, G.B. Less, A.M. Sastry, A review of conduction phenomena in Li-ion batteries, J. Power Sources 195 (2010) 7904–7929, https://doi.org/10.1016/j.jpowsour.2010.06.060.
[48] O. Chaouachi, J.-M. Réty, S. Génies, M. Chandesris, Y. Bultel, Experimental and theoretical investigation of Li-ion battery active materials properties: Application to a graphite/Ni0.6Mn0.2Co0.2O2 system, Electrochim. Acta. 366 (2021), 137428, https://doi.org/10.1016/j.electacta.2020.137428.
[49] X. Liu, Y. Wang, Y. Yang, W. Lv, G. Lian, D. Golberg, X. Wang, X. Zhao, Y. Ding, A MoS2/Carbon hybrid anode for high-performance Li-ion batteries at low temperature, Nano Energy 70 (2020), 104550, https://doi.org/10.1016/j.nanoen.2020.104550.
[50] Q. Wei, B. Shi, F. Wang, S. Shao, L. Zhu, X. Zhao, Simple and Rapid Preparation of MIL-121 with Small Particles for Lithium Adsorption from Brine, Coatings. 11 (2021) 854, https://doi.org/10.3390/coatings11070854.
[51] C. Phan, J. Shen, K. Yu, J. Liu, G. Tang, Hydrogen Bonds Topologies, Energy Frameworks and Solubilities of Five Sorafenib Salts, IJMS. 22 (2021) 6682, https://doi.org/10.3390/ijms22136682.
[52] M. Bajdich, M. García-Mota, A. Vojvodic, J.K. Nørskov, A.T. Bell, Theoretical Investigation of the Activity of Cobalt Oxides for the Electrochemical Oxidation of Water, J. Am. Chem. Soc. 135 (2013) 13521–13530, https://doi.org/10.1021/ja405997s.
[53] A. Kahn, Fermi level, work function and vacuum level, Mater. Horiz. 3 (2016) 7–10, https://doi.org/10.1039/C5MH00160A.
[54] S. Wang, J. Yu, A.M. Foley, W. Zhang, Transient Energy of an Individual Machine PART II: Potential Energy Surface, IEEE Access 9 (2021) 60223–60243, https://doi.org/10.1109/ACCESS.2021.3073117.
[55] H. Nakane, T. Kawakubo, Work function measurement of Er-oxide/W(100) surface by using of photoemission electron microscope, in: 2015 28th International Vacuum Nanoelectronics Conference (IVNC), IEEE, Guangzhou, China, 2015: pp. 110–111. https://doi.org/10.1109/IVNC.2015.7225550.
[56] V. Wang, N. Xu, J.C. Liu, G. Tang, W.-T. Geng, VASPKIT: A User-friendly Interface Facilitating High-throughput Computing and Analysis Using VASP Code, Comput. Phys. Commun. 267 (2021), 108033, https://doi.org/10.1016/j.cpc.2021.108033.
[57] M. Wang, B. Zhang, J. Ding, N. Xu, M.T. Bernards, Y. He, Y. Shi, Three-Dimensional Nitrogen-Doped Graphene Aerogel-Supported MnO Nanoparticles as Efficient Electrocatalysts for CO_2 Reduction to CO, ACS Sustainable Chem. Eng. 8 (2020) 4983–4994, https://doi.org/10.1021/acssuschemeng.0c01194.
[58] S.S. Laletina, M. Mamatkulov, E.A. Shor, V.V. Kaichev, A. Genest, I.V. Yudanov, N. Rösch, Size-Dependence of the Adsorption Energy of CO on Pt Nanoparticles: Tracing Two Intersecting Trends by DFT Calculations, J. Phys. Chem. C. 121 (2017) 17371–17377, https://doi.org/10.1021/acs.jpcc.7b05580.
[59] T. Wang, Q. Li, Q. Feng, Y. Miao, T. Li, J. Qi, F. Wei, Q. Meng, Y. Ren, B. Xiao, X. Xue, Y. Sui, Z. Sun, Carbon defects applied to potassium-ion batteries: a density functional theory investigation, Nanoscale. 13 (2021) 13719–13734, https://doi.org/10.1039/D1NR03604A.
[60] M. Endo, C. Kim, K. Nishimura, T. Fujino, K. Miyashita, Recent development of carbon materials for Li ion batteries, (2000) 15.
[61] X. Fan, W.T. Zheng, J.-L. Kuo, Adsorption and Diffusion of Li on Pristine and Defective Graphene, ACS Appl. Mater. Interfaces. 4 (2012) 2432–2438, https://doi.org/10.1021/am3000962.
[62] C. Uthaisar, V. Barone, Edge Effects on the Characteristics of Li Diffusion in Graphene, Nano Lett. 10 (2010) 2838–2842, https://doi.org/10.1021/nl100865a.